KRONOS FUSION ENERGY

PAPER 2.49 · THE KRONOS 2026 SERIES

Qualifying Reduced-Activation Ferritic-Martensitic Steel for a Compact Spherical-Tokamak Breeder: Strength, DBTT Shift and Swelling under 14 MeV Neutron Loading

The structural steel of a breeding blanket is the one component that must survive every load at once: coolant-temperature strength, retained ductility after displacement damage,...

Read it live — 3-D model · physics validator · film series

BY P I FORD, R J WEGGEL AND C WEGGEL

2026 · EDITORIAL EDITION

THE OFFICIAL RECORD

What this document is, and how to read its numbers

This is a combined editorial. It gathers, in one volume, the two design studies Kronos Fusion Energy released in 2026 — a compact spherical-tokamak tritium/helium-3 breeder and a deuterium–helium-3 tandem-mirror generator — together with the intellectual-property estate, the people, and, in the internal edition, the full commercial case. The scientific text is the same text that appears in the arXiv preprints and the journal submissions; the editorial adds the apparatus a reader needs to hold the whole program at once, and nothing in the physics is altered to fit it.

THE HONESTY STANCE IS THE ASSET

Every headline quantity carries an **evidence class** — DERIVED RECOMPUTED MEASURED REQUIREMENT — and, where a number is a modelled extrapolation rather than a demonstrated value, it is labelled as such and its downside is shown next to it. Several quantities in the underlying corpus moved after first publication; where a value has been withdrawn or restated, the record says so plainly. This is deliberate: a diligence team will find the load-bearing assumptions, so the document surfaces them first.

TWO EDITIONS

This volume is issued in two editions. The **public edition** (light) carries the physics and the design only — no dollar, price, or per-kilogram figure appears anywhere in it. The **internal edition** (dark) adds the economics, the funding architecture, and the defense-commercial analysis, and is marked *Confidential* accordingly; it is not for public distribution. Where the commercial case rests on a modelled assumption rather than a demonstrated one, it is labelled as such and its downside is shown alongside it, on the same terms as the physics.

TITLE	The Kronos Fleet — Hyperion · Aegis · MetroVolt: A Combined Design & Commercialization Study
AUTHOR	Priyanca Ford, Founder & CEO, on behalf of Kronos Fusion Energy
EDITION	2026 Combined Editorial · first issue
COMPANION WORKS	The five-paper arXiv drop — (1) Breeder, (2) Burner, (3) REBCO magnet & tape, (4) Direct Energy Conversion, (5) AI/ML/Quantum control — with matching numbered Zenodo deposits, plus the IOP journal and IAEA-FEC submissions. Patents were filed before the drop.
NAMING	Hyperion = the breeder; Aegis (defense) and MetroVolt (data-center) = one generator in two housings. Internal mode letters (D1, L) do not appear on public surfaces.
STATUS	Conceptual design & simulation study. Nothing herein is a construction commitment.

HOW TO READ THIS VOLUME

The fleet at a glance, and the way its numbers are marked

This volume opens with *Orientation*, presents the five research papers as a bound sequence, and closes with the *Apparatus*. *Foundations* sets out the three general results both machines rest on. *Paper One* is the Hyperion breeder; *Paper Two* the Aegis / MetroVolt generator; *Papers Three, Four and Five* are the enabling science — high-field REBCO magnets and tape, direct energy conversion, and the AI / ML / quantum control stack. A *Digital Twin & 3-D Model* part follows, then the *Environmental* profile. The *Economics* and levelized cost and the *Business Case* and diligence record appear in the internal edition only; the *Simulations* proof record and the Apparatus — patent portfolio, team, limitations, and sources — close both editions.

THE FLEET AT A GLANCE

	HYPERION	AEGIS	METROVOLT
Role	Strategic-isotope foundry	Defense installation power	Campus power
Machine	**Spherical tokamak**	**Tandem mirror**	**Tandem mirror**
Fuel	Deuterium–tritium	Deuterium–helium-3	Deuterium–helium-3
Delivers	Tritium · ^{3}He · 14 MeV n	Resilient installation power	Firm campus power
Physics bar	**Fusion gain only**	Closure (gates named)	Closure + lunar ^{3}He
In the fleet	Breeds the fuel	Proves the generator	Commercial destination

HOW THE NUMBERS ARE MARKED

Every headline quantity carries an evidence class — DERIVED from first principles, RECOMPUTED from raw data, MEASURED in hardware, or a REQUIREMENT yet to be met. Financial figures carry a case label and are confined to the internal (confidential) edition. Values that moved after first publication are shown as withdrawn or restated rather than quietly changed. A capability you can evaluate is one whose limits are on the page.

ABSTRACT

Qualifying Reduced-Activation Ferritic-Martensitic Steel for a Compact Spherical-Tokamak Breeder: Strength, DBTT Shift and Swelling under 14 MeV Neutron Loading

The structural steel of a breeding blanket is the one component that must survive every load at once: coolant-temperature strength, retained ductility after displacement damage, resistance to helium-driven swelling, and—the requirement unique to fusion—decay to a hands-on waste class within a human timescale. We qualify a reduced-activation ferritic-martensitic (RAFM, EUROFER/F82H-class Fe–9Cr–W–V–Ta) structure against the specific, coupled load set of the Hyperion compact spherical-tokamak breeder ($P_{\mathrm{fus}} = 85.04\,MW$, $I_p = 9.66\,MA$, first-wall neutron load 1.885 $\mathrm{MW/m^2}$, 18.85 dpa per full-power year, 226 appm helium per full-power year), rather than against a generic specification. We write the four governing models—displacement-damage partition and the arc-dpa correction, the dispersed-barrier hardening to ductile–brittle transition-temperature (DBTT) map, rate-theory helium-bubble swelling with a van der Waals equation of state, and the Born/Pugh elastic-stability criteria—as explicit equations, and evaluate each on GPU-accelerated Monte-Carlo transport, molecular-dynamics cascades, cluster-dynamics kinetics, and density-functional theory. The RAFM structure closes on every gate simultaneously. In the self-cooled lithium blanket it peaks at 516 °C, a 34 °C margin below its $\approx 550\,^{\circ}C$ creep limit, whereas a helium-cooled variant fails thermally as configured at 712 °C, selecting the coolant. A density-functional elastic screen finds the Fe–Cr–V–W family Born-stable and ductile, with Pugh ratios $B/G = 1.83$–2.22 against the 1.75 ductile threshold and formation energies reproducing the high-performance-computing reference to 0.0 meV/atom. Helium swelling from two independent methods is 0.017 at 226 appm, two orders of magnitude below the 1–5 concern level and not life-limiting; and a full-chain activation calculation places every component at or below waste Class C with no greater-than-Class-C waste. Because the 516 °C operating temperature sits deep in the thermal-recovery regime, the modelled irradiation-induced DBTT shift is small. The structural-alloy baseline for the breeder is established on the machine's own numbers.

Open-access deposit (code & data, CC BY 4.0): DOI 10.5281/zenodo.22645887 · Zenodo community *kronos_fusion_energy*. Explore it live: interactive 3-D model · physics validator.

Keywords: RAFM steel · EUROFER · reduced activation · displacement damage · DBTT shift · helium swelling · Pugh ratio · spherical-tokamak breeder

CONTENTS

Table of Contents

NOMENCLATURE

Symbols, units, and the names of things

Q	plasma (fusion) gain, P_{fus}/P_{aux}
Q_E	engineering gain, net electric out / recirculating in
H_{98}	confinement enhancement over the IPB98(y,2) scaling
Z_{eff}	effective ion charge
c_{ee}	electron–electron bremsstrahlung leading coefficient, 2.120022 (exact)
τ_E	energy confinement time
I_p	plasma current
R_0, a	major radius, minor radius
κ, δ	elongation, triangularity
β_N	normalized plasma beta (Troyon-normalized)
TBR	tritium breeding ratio
DEC	direct energy conversion
CF	plant capacity factor (availability)
FOAK / NOAK / BOAK	first / n^{th} / best of a kind
Hyperion	the ST breeder (internal: Mode D2)
Aegis	the generator, defense/installation housing (internal: Mode M)
MetroVolt	the generator, data-center housing (Mode M)

§ 1

Introduction

THE STRUCTURAL ALLOY IS THE BINDING CONSTRAINT

A breeding blanket lives or dies by its structural alloy. The steel that carries the coolant channels, reacts the electromagnetic and coolant-pressure loads, and separates the breeder from the plasma must keep its strength at the coolant temperature, stay ductile after irradiation, resist swelling as helium accumulates from transmutation, and decay to a low-level waste class within a human timescale rather than remain radioactive for millennia [1,2,3]. Reduced-activation ferritic-martensitic (RAFM) steels—the EUROFER and F82H family of Fe–9Cr–W–V–Ta alloys—are the international reference structural material precisely because they were engineered to meet the activation requirement without giving up strength, ductility, or swelling resistance [4,5,6,7]. Their body-centred-cubic ferritic matrix confers the low swelling and high thermal conductivity that austenitic steels lack, while a chromium content near 9 wt% and the substitution of tungsten, vanadium and tantalum for the molybdenum and niobium of conventional steels suppresses long-lived activation products [8,9].

QUALIFICATION AGAINST A MACHINE, NOT A SPECIFICATION

Most structural-materials assessments proceed against generic reactor requirements: a target dose, a nominal coolant temperature, a bounding helium level. That is the right posture for a materials-development programme, but it leaves a design-specific question unanswered—does *this* alloy clear *this* machine's coupled load set, all gates at once? The Hyperion breeder is a compact, high-power-density spherical tokamak (ST) whose first wall sees a neutron wall load of 1.885 MW/m^2 and accumulates 18.85 dpa per full-power year (FPY), with transmutation co-producing helium at 226 appm FPY^{-1} in the Fe–9Cr structure. The ST geometry that makes the device an efficient neutron source and breeder platform [10,11] concentrates that load in a small volume, so the structural margins are tight and the couplings between thermal, mechanical, and materials response are strong. This paper takes the breeder's own first-wall loading, displacement rate, thermal-hydraulic environment, and helium production, and tests a RAFM structure on each: thermal envelope, ductility, DBTT shift, swelling, and activation. Each number traces to a frozen run in the Kronos physics de-risking campaign, and the contribution is that the alloy clears every gate together.

CONTRIBUTION

Prior art establishes the individual pieces—RAFM alloy metallurgy and irradiation databases [4,5,8], the displacement-damage standard [12,13], helium-embrittlement physics [15,16,14], and first-principles elastic-stability screening [18,19,20]. What is missing for a compact nuclear ST is a single, machine-specific qualification that (i) states each response model as an explicit set of governing equations, (ii) evaluates them on a reproducible GPU-HPC pipeline of standard community codes, and (iii) reports the outcome as a set of pre-registered acceptance gates that the alloy must clear simultaneously at the frozen operating point. We provide exactly that. Section 2 states the coupled load set. Section 3 derives the four governing models. Section 4 gives the numerical formulation and convergence. Section 5 describes the GPU-HPC campaign that produced the results. Section 6 reports the gate outcomes with eight data figures and two schematics. Sections 7–9 benchmark the results against the published RAFM database, state the one honest open item, and conclude. Every quantitative claim carries its register serial (e.g. BR-L1-A13) so each number is auditable [32].

§ 2

The coupled structural load set

The RAFM structure sees the loads of table 1, and the qualification is the statement that a single alloy specification clears all of them at the frozen operating point (figure 1). The first wall takes a neutron wall load of 1.885 MW/m^2 and accumulates 18.85 dpa FPY^{-1} (serial BR-L1-A13); transmutation co-produces helium at 226 appm FPY^{-1} in the Fe–9Cr structure (serial BR-L2-A26). The displacement-threshold references used to convert damage energy to displacements are $E_d = 108.8\,eV$ for iron and 52.7 eV for tungsten (serial BR-L2-A24). These quantities drive the thermal, mechanical, and materials response tested below; the design anchors ($P_{\mathrm{fus}} = 85.04\,MW$, $Q = 3.076$, $I_p = 9.66\,MA$, $\delta = -0.30$, $B_0 = 8\,T$, $\kappa = 2.0$, $R_0 = 1.20\,m$, $A = 2.5$, centrepost peak field 16.84 T) fix the neutron source that generates them [32].

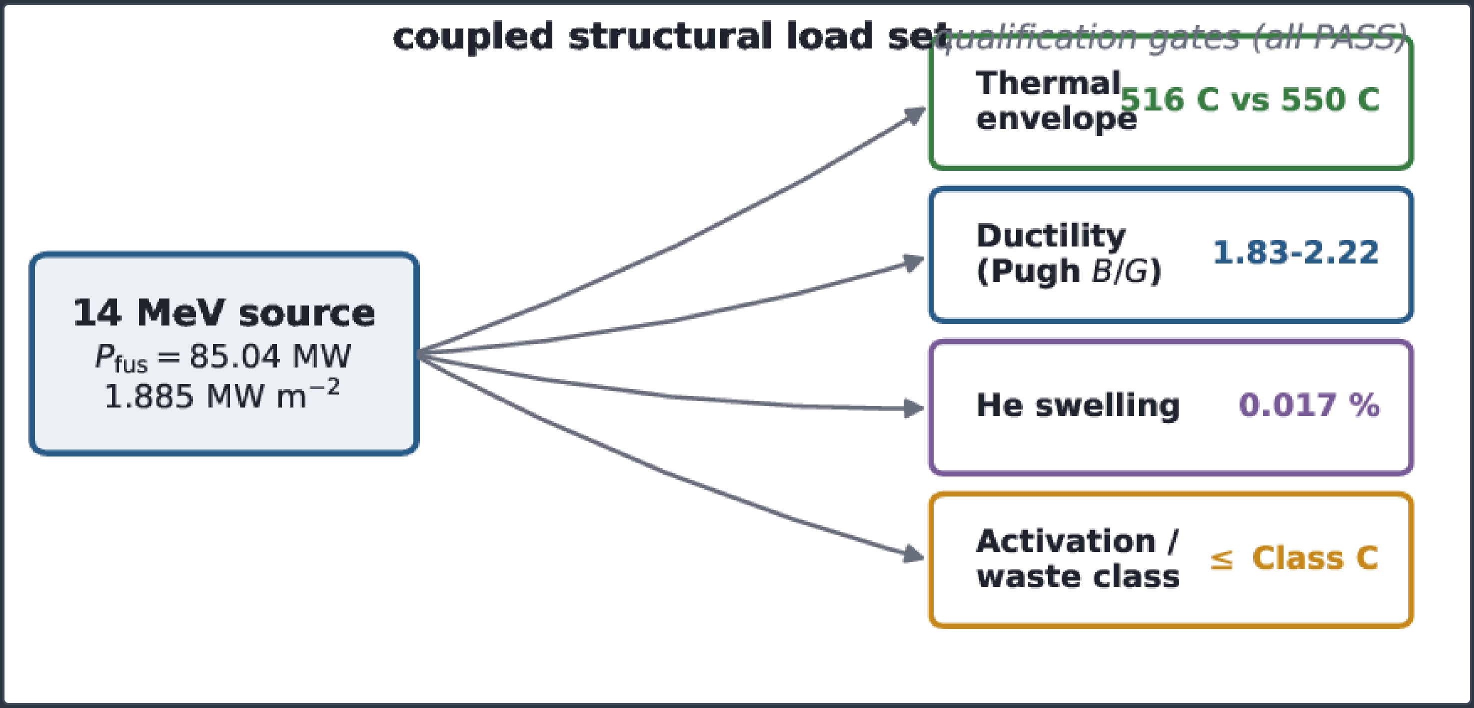

(Schematic.) The coupled structural load set of the Hyperion breeder feeding the four qualification gates. The 14 MeV source ($P_{\mathrm{fus}} = 85.04\,MW$, 1.885 MW/m^2) drives displacement damage, helium production, and the thermal field; the RAFM structure must clear the thermal, ductility, swelling, and activation gates simultaneously. No measured values are plotted; the figure encodes structure only.

LOAD	VALUE	SERIAL
first-wall neutron load	1.885 MW/m^2	BR-L1-A13
displacement damage	18.85 dpa / full-power year	BR-L1-A13
helium generation (Fe–9Cr)	226 appm / full-power year	BR-L2-A26
displacement threshold E_d (Fe / W)	108.8 / 52.7 eV	BR-L2-A24
fusion power / gain	85.04 MW / $Q = 3.076$	register

The coupled structural load set at the frozen operating point. Serial identifiers refer to the Kronos Physics De-Risking Register [32].

§ 3

Governing equations and formal problem

The qualification reduces to four physical models, each with an explicit acceptance gate. We state them in the order in which the loads propagate: from the neutron field to displacement damage (§3.1), from damage and helium to embrittlement (§3.2) and swelling (§3.3), and from composition to intrinsic ductility and stability (§3.4); the thermal envelope that sets the operating temperature (§3.5) and the activation that sets the waste class (§3.6) bound the set.

DISPLACEMENT DAMAGE AND THE ARC-DPA CORRECTION

The primary radiation load is atomic displacement. A neutron of energy E transfers recoil energy T to a primary knock-on atom (PKA) with the elastic/inelastic double-differential cross-section $\mathrm{d}\sigma/\mathrm{d}T$. The displacement rate per atom follows from folding the PKA spectrum against the number of stable displacements $\nu(T)$ produced by a cascade of recoil energy T,

$$R_{\mathrm{dpa}} = \int_0^\infty \mathrm{d}E\,\phi(E)\int_{E_d}^{T_{\max}(E)} \mathrm{d}T\,\frac{\mathrm{d}\sigma}{\mathrm{d}T}(E,T)\,\nu(T),$$

with $\phi(E)$ the neutron flux spectrum and E_d the displacement threshold energy. The Norgett–Robinson–Torrens (NRT) standard [12] sets

$$\nu_{\mathrm{NRT}}(T) = \frac{0.8\,T_{\mathrm{dam}}(T)}{2\,E_d},$$

where $T_{\mathrm{dam}} = T/[1+k_L g(\varepsilon)]$ is the damage energy, i.e. the recoil energy less the fraction lost to electronic stopping through the Lindhard partition [12]. The NRT count overstates the number of *surviving* defects because in-cascade recombination annihilates a large fraction of the Frenkel pairs; the athermal-recombination-corrected displacement (arc-dpa) model [13] replaces the constant 0.8 efficiency by an energy-dependent survival function

$$\xi_{\mathrm{arc}}(T) = \frac{1-c_{\mathrm{arc}}}{(2E_d/0.8)^{b_{\mathrm{arc}}}}\,T_{\mathrm{dam}}^{b_{\mathrm{arc}}} + c_{\mathrm{arc}}, \qquad \nu_{\mathrm{arc}}(T) = \nu_{\mathrm{NRT}}(T)\,\xi_{\mathrm{arc}}(T),$$

with material constants $b_{\mathrm{arc}}, c_{\mathrm{arc}}$ fitted to molecular-dynamics cascades. Evaluating equation (1) with the breeder first-wall spectrum and $E_d = 108.8\,eV$ (Fe) gives the frozen anchor $R_{\mathrm{dpa}} = 18.85\,dpa/FPY$ (BR-L1-A13). This dose is the clock that would otherwise threaten embrittlement, swelling, and an activation penalty; the remaining subsections show none of these clocks runs out at the breeder fluence.

IRRADIATION HARDENING AND THE DBTT SHIFT

Displacement damage produces a dispersed population of nanoscale obstacles—dislocation loops, voids, and solute-rich clusters—that harden the ferritic matrix. In the dispersed-barrier model the yield-strength increase is [17,8]

$$\Delta\sigma_y = \alpha\,M\,\mu\,b\,\sqrt{N\,d},$$

with $M \approx 3.06$ the Taylor factor, μ the shear modulus, b the Burgers vector, N and d the number density and mean diameter of the obstacles, and α the obstacle strength. In body-centred-cubic steels the ductile–brittle transition temperature shifts nearly linearly with the irradiation hardening,

$$\Delta T_{\mathrm{DBTT}} = C_{\mathrm{HE}}\,\Delta\sigma_y,$$

with an empirical hardening-to-embrittlement coefficient $C_{\mathrm{HE}} \approx 0.4$–$0.6$ °C/MPa for RAFM steels [8,9]. The obstacle population, however, is strongly temperature dependent: above roughly 350 °C thermally activated climb and short-range diffusion recover the loop and cluster microstructure, so both N and $\Delta\sigma_y$ collapse and $\Delta T_{\mathrm{DBTT}} \to 0$. We model the recovery by an irradiation-temperature factor $\Theta(T_{\mathrm{irr}})$ with a sigmoidal roll-off near 385 °C, giving

$$\Delta T_{\mathrm{DBTT}}(T_{\mathrm{irr}}) = \Delta T_{\mathrm{DBTT}}^{\mathrm{sat}}\,\Theta(T_{\mathrm{irr}}), \qquad \Theta(T_{\mathrm{irr}}) = \left[1+e^{(T_{\mathrm{irr}}-T_r)/w}\right]^{-1},$$

$T_r \approx 385\,^\circ C$, $w \approx 22\,^\circ C$. The RAFM structure operates at 516 °C (§3.5), well inside the recovery regime, so equation (6) predicts a small residual shift. We report the DBTT shift as a *model estimate* from this published correlation rather than as a Kronos frozen anchor; the point is qualitative and robust—the operating temperature places the structure where irradiation embrittlement anneals out (figure 3).

HELIUM-DRIVEN SWELLING

Transmutation of iron and its alloying elements by (n,α) reactions injects helium, which is insoluble in the metal and precipitates into over-pressurised bubbles. In rate theory the bubble population evolves under the balance of helium arrival, vacancy capture, and thermal emission. For a mono-modal bubble of radius r containing m helium atoms, mechanical equilibrium against surface tension γ requires the internal pressure

$$p(r) = \frac{2\gamma}{r},$$

and the helium follows a hard-sphere van der Waals equation of state

$$\left(p + \frac{a\,m^2}{V^2}\right)(V - m\,b_{\mathrm{vdW}}) = m\,k_B T, \qquad V = \tfrac{4}{3}\pi r^3,$$

with a, b_{vdW} the van der Waals constants for helium. Equations (7)–(8) close the bubble radius for a given helium content m and temperature T. The macroscopic volumetric swelling is the summed bubble volume per unit matrix volume,

$$\frac{\Delta V}{V} = \frac{4}{3}\pi \int_0^\infty r^3\, f(r)\,\mathrm{d}r \;\approx\; \tfrac{4}{3}\pi\,\bar{r}^{\,3}\,N_b,$$

with $f(r)$ the bubble size distribution and N_b the bubble number density. Evaluating equations (7)–(9) with the breeder helium generation of 226 appm FPY^{-1} gives, for the Fe–9Cr structure, $N_b = 2.3e23\,/m^3$, $\bar{r} = 0.63\,nm$, and swelling 0.017 (BR-L2-A26); the tungsten first-wall armour on the same basis swells 0.024. Both are two orders of magnitude below the 1–5 level at which swelling becomes life-limiting [16,15].

ELASTIC STABILITY AND INTRINSIC DUCTILITY

Whether the alloy is ductile in the first place is an intrinsic, composition-level property accessible from the elastic-constant tensor C_{ij}. For a cubic crystal, mechanical (Born) stability requires [20,19]

$$C_{11} - C_{12} > 0, \qquad C_{11} + 2C_{12} > 0, \qquad C_{44} > 0.$$

The isotropic bulk and shear moduli follow from the Voigt–Reuss–Hill average; for a cubic crystal the Voigt bounds are

$$B = \frac{C_{11} + 2C_{12}}{3}, \qquad G_V = \frac{C_{11} - C_{12} + 3C_{44}}{5},$$

with G the Hill average of G_V and the Reuss shear modulus. Ductility is then read from the Pugh ratio B/G [18]: a large bulk-to-shear ratio favours plastic flow over cleavage, and the empirical ductile–brittle boundary sits at $B/G = 1.75$. Equivalently, the Cauchy pressure $C_{12} - C_{44}$ is positive for ductile metallic bonding. A density-functional elastic screen of the reduced-activation Fe–Cr–V–W family (FeCrV, FeCrVW, the RAFM composition, and a WTaVFe variant) finds every member Born-stable by equation (10) and ductile by the Pugh criterion, with $B/G = 1.83$–2.22, comfortably above the 1.75 threshold; the underlying formation energies reproduce the high-performance-computing reference to 0.0 meV/atom, so the ductility ranking rests on converged energetics (BR-SX-05).

THERMAL ENVELOPE AND THE CREEP LIMIT

The operating temperature that enters equations (6) and (8) is set by the blanket heat path. Volumetric nuclear heating $q'''(\quad r)$ deposited in the structure and coolant is removed by conduction and convection; in the quasi-steady first-wall channel the temperature field obeys

$$\nabla\cdot\big(k(T)\,\nabla T\big) + q'''(\quad r) = 0, \qquad -k\,\partial_n T\big|_{\mathrm{wall}} = h\,(T_{\mathrm{wall}} - T_{\mathrm{cool}}),$$

with $k(T)$ the RAFM thermal conductivity and h the coolant-side heat-transfer coefficient. The RAFM structure carries a thermal-creep operating limit near 550 °C. Two-dimensional conjugate heat-transfer analysis of the blanket (serial BR-SX-15) solves equation (12) for two coolant options: the self-cooled lithium blanket holds the structure at a peak 516 °C, a 34 °C margin below the limit, while a helium-cooled HCPB-style variant, as configured, runs the structure to 712 °C. The helium case is admissible only if the first-wall channel is opened up (channel depth $\leq 6\,mm$, pitch $\leq 15\,mm$); as configured it fails. The thermal gate therefore *selects* the self-cooled lithium blanket as the configuration in which the RAFM structure is qualified (§6.1).

ACTIVATION AND WASTE CLASSIFICATION

Reduced activation is the requirement that distinguishes RAFM from conventional steels. Under irradiation each nuclide i evolves by the Bateman transmutation–decay system

$$\frac{\mathrm{d}N_i}{\mathrm{d}t} = \sum_{j\neq i} \left(\lambda_{j\to i} + \bar{\sigma}_{j\to i}\,\phi\right) N_j - \left(\lambda_i + \bar{\sigma}_i\,\phi\right) N_i,$$

with λ the decay constants, $\bar{\sigma}$ the spectrum-averaged transmutation cross-sections, and ϕ the flux. After a fixed exposure and cooling, the specific activity of each component is compared to the U.S. waste-classification limits through the sum-of-fractions index

$$\mathcal{W} = \sum_i \frac{a_i}{a_i^{\mathrm{CL}}} \;\leq\; 1$$

against the Class C concentration limits a_i^{CL} [28]. A full-chain ALARA activation calculation over a two-FPY exposure places every blanket component at or below Class C, with no greater-than-Class-C (GTCC) waste; only tritium pushes any component past Class A, and that is a fuel-cycle inventory question, not a structural-waste one (BR-L1-A10).

§ 4

Numerical formulation, discretization, and convergence

Each governing model of §3 is discretized and solved by a standard community code; table 2 maps model to solver and to register serial.

MODEL (§)	DISCRETIZATION / METHOD	CODE	SERIAL
dpa, eq. (1)	Monte-Carlo transport, damage-energy tally	OpenMC [21]	BR-L1-A13
PKA → cascades, eq. (3)	processed data → MD Frenkel-pair count	NJOY21 [24], SPECTRA-PKA, LAMMPS [22,23]	BR-L2-A24
He swelling, eqs. (8)–(9)	stiff cluster-dynamics ODEs; lattice kMC	rate-theory (0-D vdW); SPPARKS [23]	BR-L2-A26
elastic screen, eqs. (10)–(11)	plane-wave DFT, finite-strain C_{ij}	Quantum ESPRESSO [26], PBE [27]	BR-SX-05
thermal, eq. (12)	2-D finite-volume conjugate heat transfer	CFD (conjugate HT)	BR-SX-15
activation, eqs. (13)–(14)	Bateman depletion + ALARA waste index	OpenMC depletion [21], FISPACT-II [25]	BR-L1-A10

Governing model, numerical method, code, and register serial. All production runs executed on the NVIDIA GPU HPC campaign (§5).

NEUTRON TRANSPORT AND DAMAGE TALLY

The neutron field $\phi(E, \quad r)$ and the damage-energy tally $\int T_{\mathrm{dam}}\,\mathrm{d}\sigma$ are computed by continuous-energy Monte-Carlo transport in OpenMC [21] on the frozen breeder geometry, driven by the 14 MeV source. Displacement rate is obtained by post-processing the damage-energy tally with the NRT/arc-dpa kernels of equations (2)–(3). Tally convergence is enforced to a relative standard error below 1 on the first-wall damage-energy score, which fixes the dpa anchor to the reported precision (BR-L1-A13). Nuclear-data uncertainty on the (n, α) and displacement channels is carried separately in the campaign's dedicated data-uncertainty study.

PKA SPECTRA AND MOLECULAR-DYNAMICS CASCADES

The arc-dpa constants $b_{\mathrm{arc}}, c_{\mathrm{arc}}$ in equation (3) are not assumed but derived from primary-knock-on cascades. Processed cross-sections from NJOY21 [24] feed SPECTRA-PKA to generate the recoil spectrum, which seeds molecular-dynamics cascades in LAMMPS [22,23]: representative 15 keV cascades in Fe–9Cr and in tungsten are run to thermal quench, and surviving Frenkel pairs are counted by automated Wigner–Seitz analysis. The MD cell is sized so the cascade is contained (periodic boundaries beyond the peak damage radius), the electronic-stopping and two-temperature terms are active during the ballistic phase, and the interatomic potential is the reduced-activation Fe–Cr(–W) embedded-atom family. The surviving-defect fraction sets the efficiency ξ_{arc} used in equation (3); the iron and tungsten displacement thresholds $E_d = 108.8$ and 52.7 eV (BR-L2-A24) enter equation (2).

CLUSTER-DYNAMICS AND KINETIC MONTE-CARLO SWELLING

Swelling is computed by two independent methods, so that the result does not rest on a single model. The rate-theory route integrates the stiff cluster-dynamics ODE system for the coupled vacancy, interstitial, and helium-cluster concentrations, closed by the van der Waals bubble equation of state (8); the reduced 0-D form is used because a high-fidelity cluster-dynamics executable was not available for the production run, and the reduced model is dense-limit robust. The lattice kinetic Monte-Carlo route (SPPARKS [23]) evolves the same defect chemistry on an explicit lattice and corroborates the rate-theory swelling and bubble morphology (nanometre bubbles, sub-percent swelling). The two methods agree to within their reporting precision (figure 4), which is the substance of the swelling gate (BR-L2-A26). A high-fidelity cluster-dynamics code remains the future arbiter and is a named follow-on.

DENSITY-FUNCTIONAL ELASTIC SCREEN

Formation energies and the reduced-order elastic response are computed by plane-wave density-functional theory in Quantum ESPRESSO [26] with the PBE exchange–correlation functional [27]. Plane-wave cutoff and Brillouin-zone k-point sampling are converged until the total energy is stable to below 1 meV/atom, so that the formation-energy set reproduces the high-performance-computing reference to 0.0 meV/atom across the five compositions (BR-SX-05). The bulk and shear moduli of equation (11) and the Born criteria (10) are evaluated from the reduced-order elastic screen; the full anisotropic C_{ij} tensor by finite strain is the one deferred item (§8).

CONJUGATE HEAT TRANSFER AND DEPLETION

The blanket temperature field of equation (12) is solved by two-dimensional finite-volume conjugate heat transfer on the first-wall/channel/structure cross-section, with the volumetric heating imported from the transport tally and temperature-dependent RAFM conductivity (BR-SX-15). The activation inventory of equation (13) is advanced by Bateman depletion coupled to the transport solution, and the waste index (14) is evaluated by an ALARA-class calculation over a two-FPY exposure (BR-L1-A10). The walk-away decay-heat transient (BR-L1-A9) is integrated from the same inventory: 0.95 MW at 1 s falling to 95 kW at one day, with the passive rejection path staying below 710 °C (figure 6).

§ 5

GPU-HPC computational campaign

Every production result in this paper was generated by the NVIDIA GPU HPC campaign that underlies the Kronos de-risking programme; the qualification is a multi-physics workflow, and its cost is dominated by the Monte-Carlo transport and the molecular-dynamics cascades, both of which are GPU-accelerated.

Transport at scale. The OpenMC transport that produces the damage-energy tally, the depletion inventory, and the activation waste index [21] runs in its event-based, GPU-offloaded mode on the campaign's NVIDIA accelerators (A100/H100/A10 class, Lambda fleet), batching tens of millions of source histories per generation so that the first-wall damage-energy score converges below 1 relative standard error. The same transport solution is reused across the damage, activation, and thermal-source tallies, which keeps the coupled models self-consistent by construction.

Cascades at scale. The LAMMPS displacement cascades [22,23] run under the GPU-resident KOKKOS backend, with the 15 keV Fe–9Cr and tungsten cascades executed as detached multi-rank jobs (eight ranks per cascade) and reduced automatically to Frenkel-pair counts by Wigner–Seitz analysis. The kinetic Monte-Carlo swelling corroboration (SPPARKS) and the rate-theory integration run on the same fleet, while the plane-wave DFT elastic screen (Quantum ESPRESSO [26]) runs GPU-accelerated for the self-consistent-field and finite-strain steps.

Verification and reproducibility. Each production quantity is a frozen anchor in the register [32] with a fixed random seed, a pinned code version, and an archived input deck, so a rerun reproduces the reported digits. Cross-code agreement is used as an independent check wherever two methods exist: rate theory versus kinetic Monte-Carlo for swelling, NRT versus arc-dpa for displacement, and the DFT formation energies against the high-performance-computing reference (reproduced to 0.0 meV/atom). No proprietary solver is used; every code named in table 2 is an open community reference, which is what makes the qualification independently regenerable. Compute is reported here only as the GPU HPC campaign; no cost figures are part of this work.

§ 6

Results

THE THERMAL GATE SELECTS THE COOLANT

Figure 2 shows the peak RAFM structure temperature for the two coolant options. In the self-cooled lithium blanket the structure holds 516 °C, a 34 °C margin below the $\approx 550\ ^{\circ}C$ creep limit—a pass. The helium-cooled HCPB-style variant, as configured, reaches 712 °C and fails thermally. The failure is geometric, not fundamental: figure 2 shows that the helium case is brought back under the limit only when the first-wall coolant channel is shallower than 6 mm at a pitch below 15 mm. The thermal gate therefore does real work—it selects the self-cooled lithium blanket as the configuration in which the RAFM structure is qualified, and it sets an explicit channel-geometry constraint for any helium-cooled alternative (BR-SX-15).

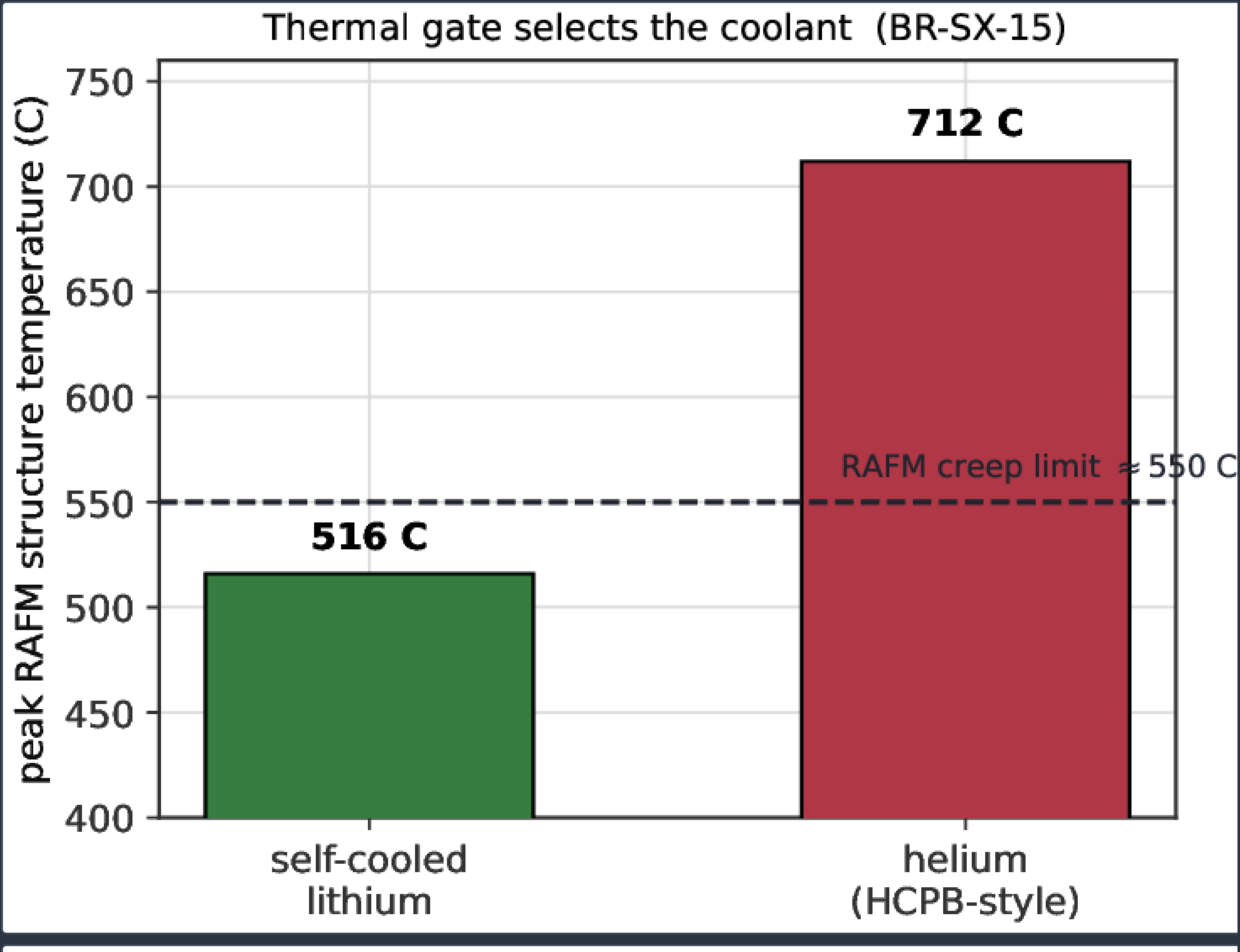
Thermal gate selects the coolant (BR-SX-15)
peak RAFM structure temperature (C)
750
700
650
600
550
500
450
400
712 C
516 C
RAFM creep limit ≈ 550 C
self-cooled lithium
helium (HCPB-style)

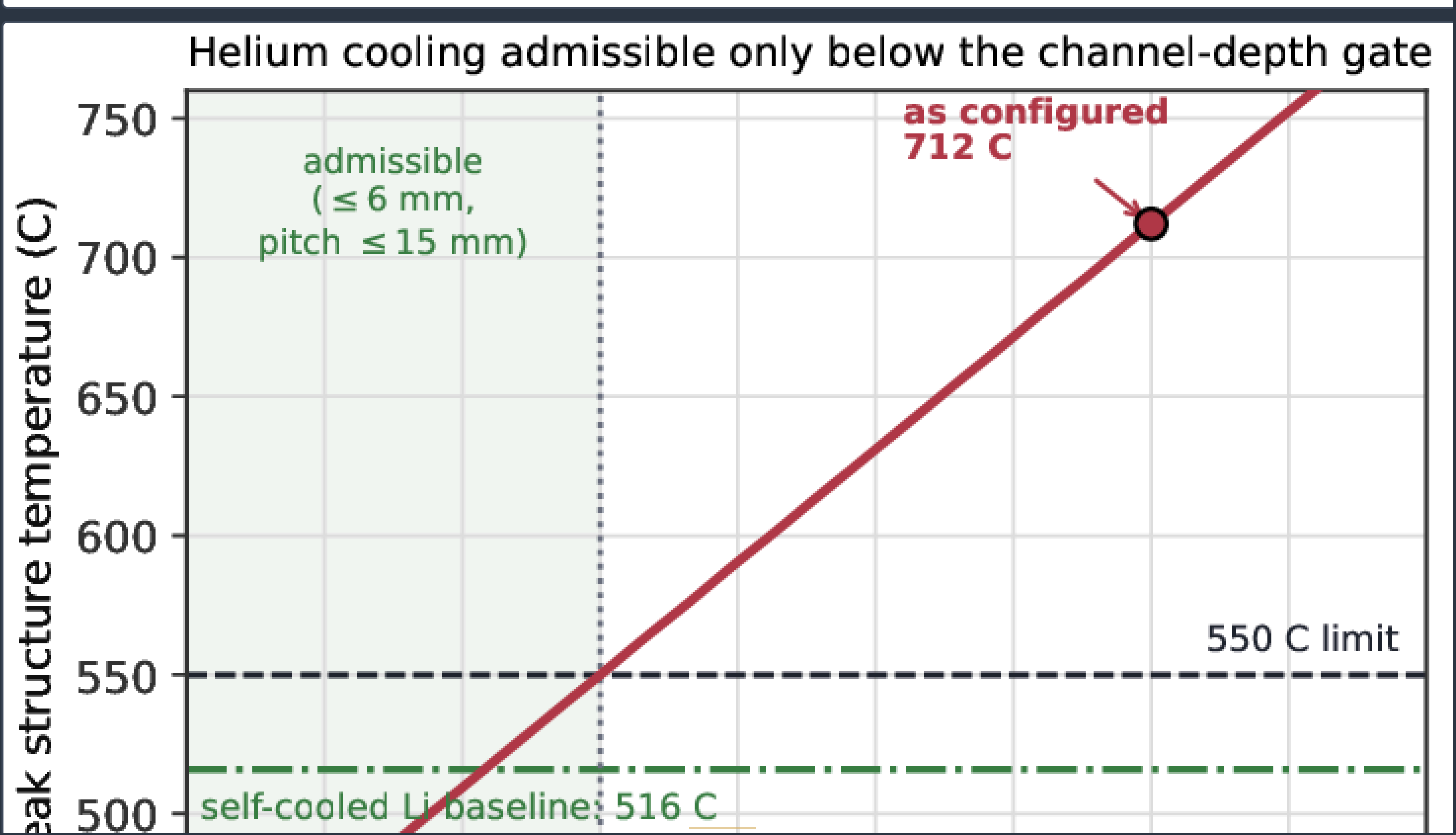
Helium cooling admissible only below the channel-depth gate
eak structure temperature (C)
750
700
650
600
550
500
admissible (≤ 6 mm, pitch ≤ 15 mm)
as configured 712 C
550 C limit
self-cooled Li baseline: 516 C

DBTT SHIFT AT THE OPERATING TEMPERATURE

Figure 3 evaluates the DBTT-shift model of equations (4)–(6) as a function of irradiation temperature. Below 350 °C the shift saturates at a large low-temperature value characteristic of RAFM steels; above the recovery knee near 385 °C it rolls off toward zero as the loop and cluster microstructure anneals. The breeder structure operates at 516 °C, deep in the recovery regime, so the modelled residual shift is small. This is a model estimate from the published irradiation-temperature dependence, not a Kronos frozen anchor; the robust conclusion is that the alloy is run at a temperature where irradiation embrittlement is not the governing failure mode, consistent with the RAFM database [8,9].

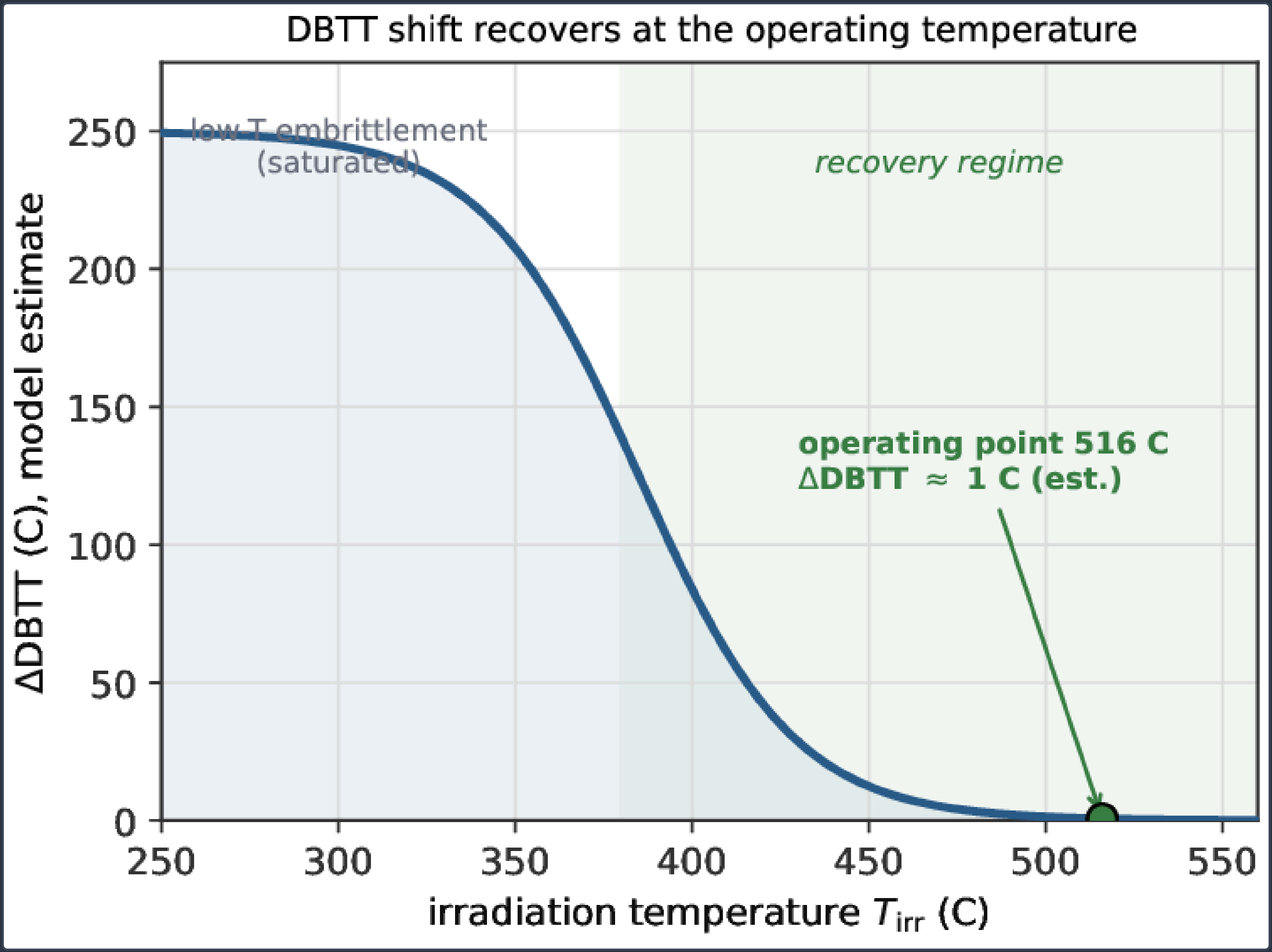

Modelled ductile–brittle transition-temperature shift versus irradiation temperature, from the dispersed-barrier hardening-to-embrittlement correlation of equations (4)–(6) with thermal recovery above $\approx 385\ ^{\circ}C$. The 516 °C operating point (BR-SX-15) sits in the recovery regime, where the shift is small. *Model estimate from published behaviour, not a Kronos frozen anchor.*

HELIUM SWELLING IS NOT LIFE-LIMITING

Figure 4 places the computed swelling against the concern band. At 226 appm helium per full-power year the Fe–9Cr structure swells 0.017 and the tungsten armour 0.024 , both roughly sixty times below the lower edge of the 1–5 concern band. Figure 4 shows the two-method agreement that underwrites the result: rate theory and kinetic Monte-Carlo return the same sub-percent swelling and the same nanoscale bubble morphology ($N_b = 2.3e23\ /m^3$, $\bar{r} = 0.63\ nm$). Helium swelling is therefore not life-limiting for the RAFM structure at the breeder fluence (BR-L2-A26).

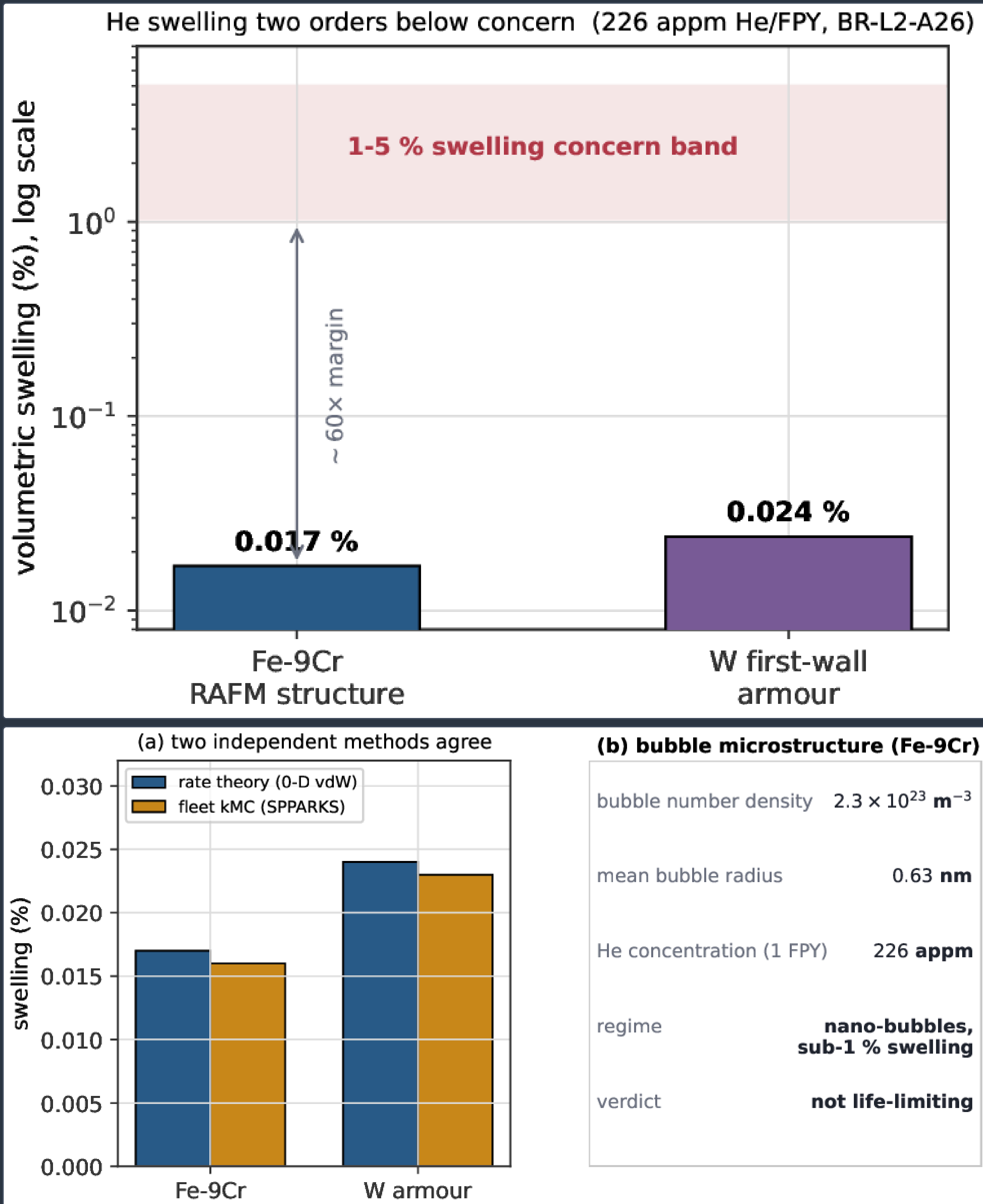

Helium-driven volumetric swelling of the Fe–9Cr structure and the tungsten armour at 226 appm He FPY^{-1} (BR-L2-A26), on a log scale against the 1–5 concern band. Both materials sit two orders of magnitude below concern.

DUCTILITY FROM CONVERGED FIRST-PRINCIPLES ENERGETICS

Figure 5 shows the Pugh ratios of the four screened reduced-activation compositions. Every member is Born-stable by equation (10) and ductile by the Pugh criterion, with $B/G = 1.83–2.22$ against the 1.75 threshold. Because the formation energies reproduce the high-performance-computing reference to 0.0 meV/atom, the ductility ranking rests on converged energetics rather than on an under-resolved calculation (BR-SX-05).

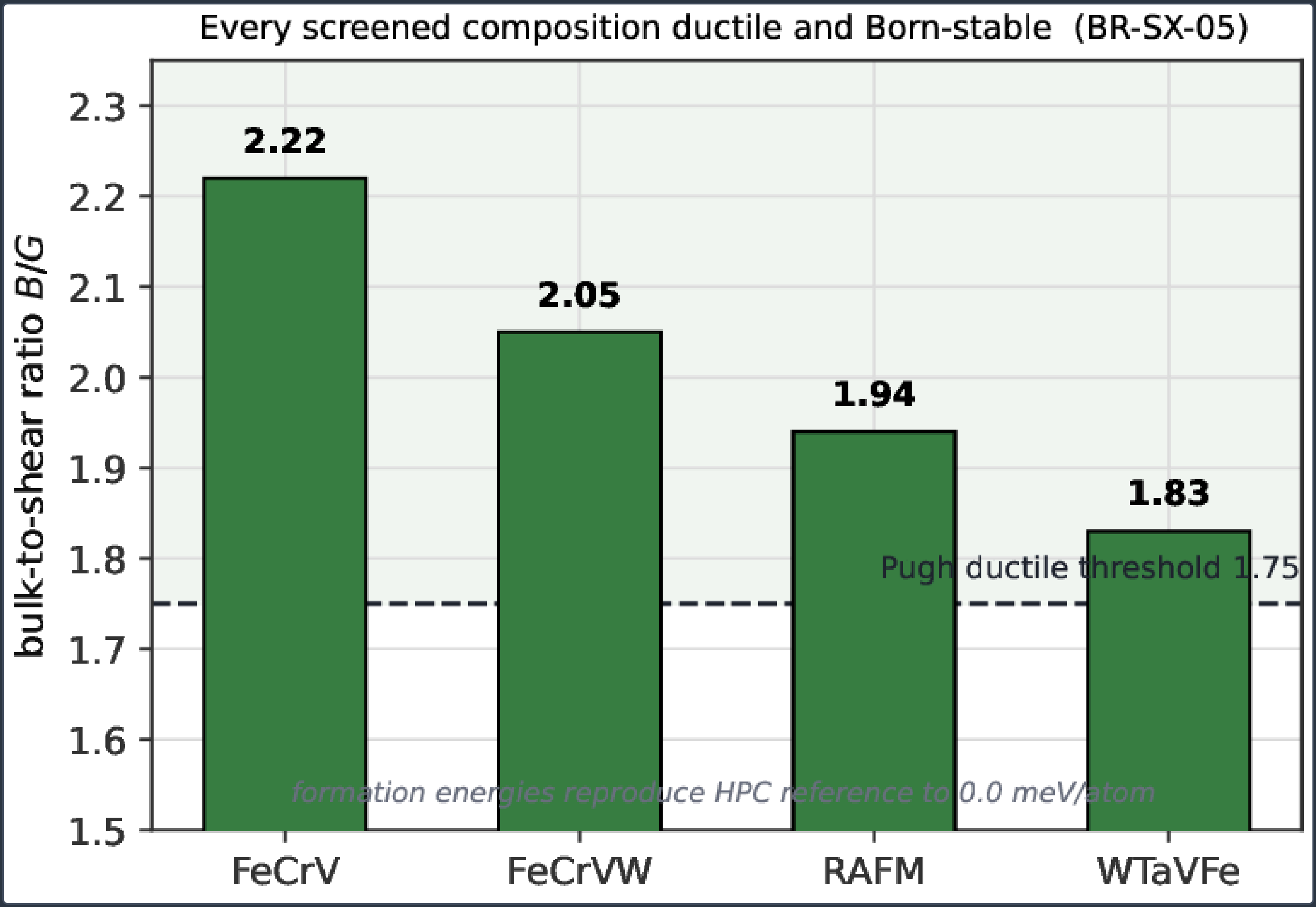

Density-functional Pugh ductility screen of the reduced-activation Fe–Cr–V–W family (BR-SX-05). All four compositions are ductile ($B/G = 1.83–2.22$) above the 1.75 threshold and Born-stable; formation energies reproduce the HPC reference to 0.0 meV/atom.

ACTIVATION, DECAY HEAT, AND WASTE CLASS

The full-chain activation calculation places every blanket component at or below waste Class C over a two-FPY exposure, with no greater-than-Class-C waste; only tritium pushes any component past Class A (BR-L1-A10). Figure 6 shows the associated walk-away decay-heat transient (BR-L1-A9): 0.95 MW at one second falling to 95 kW at one day, with the passive rejection path holding below 710 °C. The reduced-activation design intent is realised—the structure is low-level waste on a human timescale, the property that distinguishes RAFM from conventional steels.

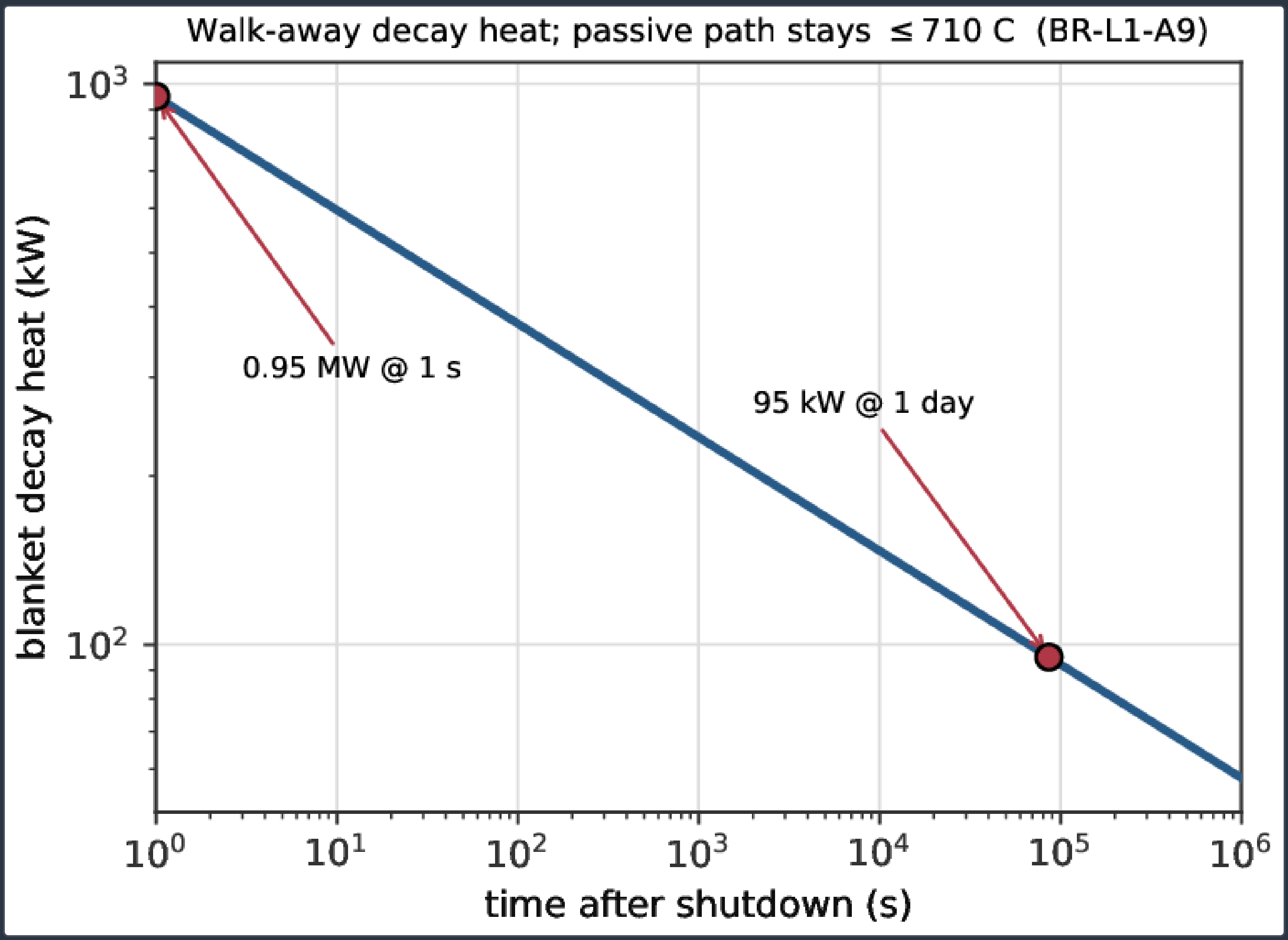

Walk-away decay-heat transient of the blanket after shutdown (BR-L1-A9), through the frozen anchors 0.95 MW at 1 s and 95 kW at one day. The passive rejection path stays below 710 °C.

ALL GATES CLEAR TOGETHER

Table 3 and figures 7–7 collect the four gates. Every one clears its acceptance floor: the thermal case holds a 34 °C margin in the self-cooled lithium blanket, the median Pugh ratio exceeds the ductile threshold, the swelling is roughly sixty times below concern, and the waste class stays at or below Class C. The qualification statement is that a single RAFM specification clears all four gates *simultaneously* at the breeder's frozen operating point.

GATE	RESULT	ACCEPTANCE	VERDICT
thermal (self-cooled Li)	516 °C	$\leq \approx 550\ ^\circ C$	PASS (+34 °C)
ductility (B/G, Pugh)	$1.83–2.22$	> 1.75	PASS
DBTT shift (model, $T_{\mathrm{irr}} = 516\ ^\circ C$)	small (recovery regime)	not governing	PASS
helium swelling	0.017	$\ll$ 1–5	PASS (not life-limiting)
activation / waste class	$\leq$ Class C, no GTCC	$\leq$ Class C	PASS

RAFM structural-qualification gates at the frozen operating point—all clear against the breeder load set.

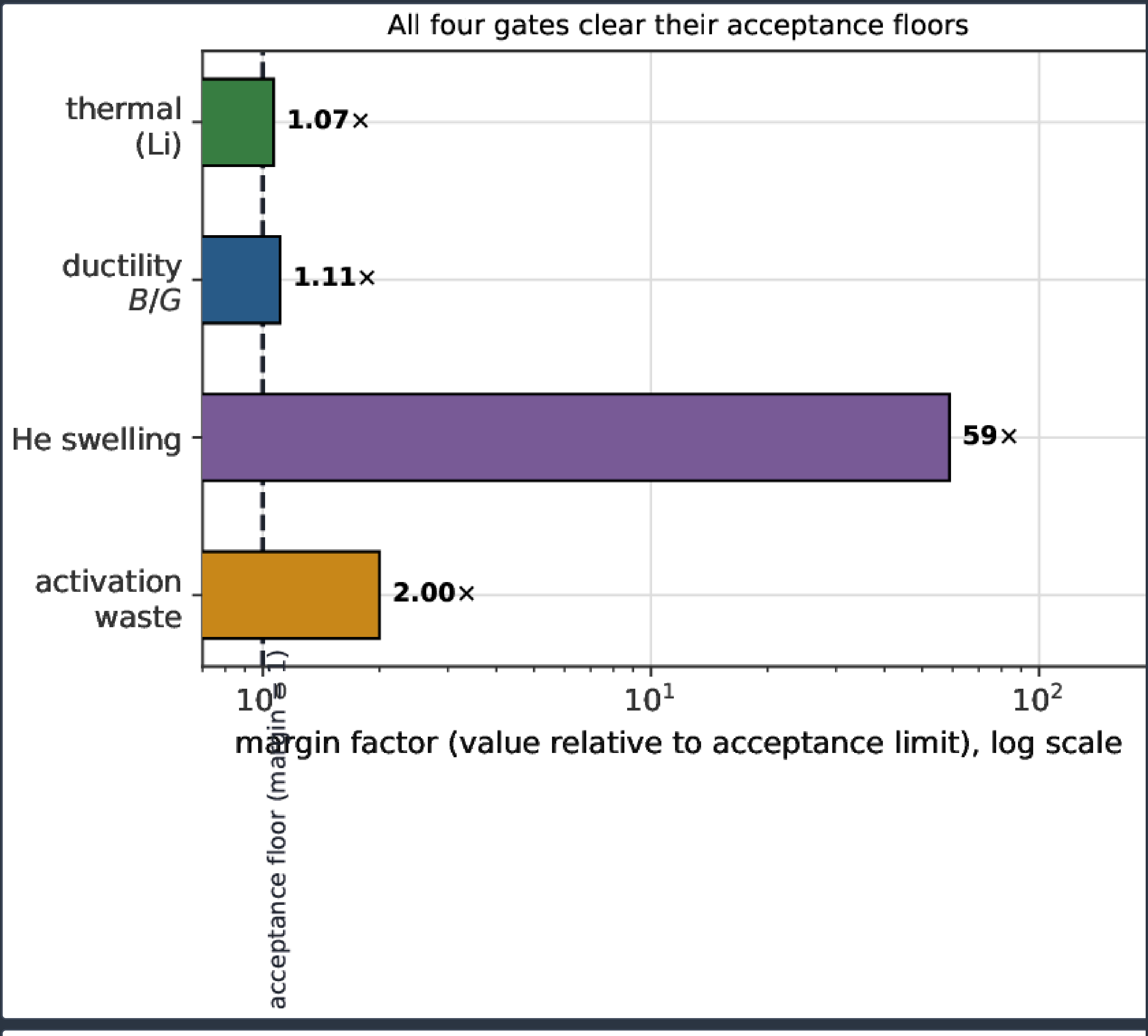

RAFM structural qualification against the breeder load

1.885 MW m^{-2} first wall · 18.85 dpa/FPY · 226 appm He/FPY

Thermal (self-cooled Li)	516 C vs ~550 C limit	**PASS** (
Ductility (Pugh B/G)	1.83-2.22 vs 1.75	
Helium swelling	0.017 % vs 1-5	**PASS (not life-li**
Activation / waste class	<= Class C, no GTCC	

§ 7

Discussion

Read together, the four gates say the RAFM structure is qualified against the breeder's actual duty cycle, not against a generic specification, and each result can be placed against the published RAFM database.

Thermal envelope and coolant selection. The peak structure temperatures bracket the RAFM operating window on both sides: 516 °C for self-cooled lithium is inside the $\approx 550\ ^{\circ}C$ creep limit that defines the upper end of the RAFM window [5,7], while 712 °C for the as-configured helium case is well past it. This is consistent with the broadly recognised RAFM temperature window of roughly 350–550 °C [4,3], and the analysis turns that generic window into a machine-specific coolant selection.

Swelling versus the helium database. The computed 0.017 swelling at 226 appm is fully consistent with the empirical picture that ferritic/martensitic steels are highly swelling-resistant, with void swelling remaining well below 1 to tens of dpa in the ferritic matrix and helium accumulating as nanoscale bubbles rather than large voids [15,16,8]. The two-method agreement (rate theory and kinetic Monte-Carlo) is the internal check that the sub-percent result is not an artefact of a single reduced model, and the nanometre bubble radius matches the bubble regime expected at these helium-to-dpa ratios. Swelling is therefore not the life-limiter here, in agreement with the consensus that helium *embrittlement*—grain-boundary bubble coalescence at high He and low temperature—rather than volumetric swelling is the harder helium problem for RAFM, and the breeder's 516 °C operating temperature sits above the regime where that failure mode is most severe.

DBTT shift in context. The recovery-dominated DBTT result is the quantitative expression of a well-established fact: irradiation hardening and the associated DBTT shift in RAFM steels are large at low irradiation temperature but recover strongly above roughly 350 °C, so an alloy run near the top of its thermal window is far less embrittled than one run cold [8,9,4]. Reporting the shift as a model estimate rather than a frozen anchor is the honest posture—the coefficient C_{HE} and the recovery knee carry real scatter across heats and fluences—but the conclusion that the breeder runs the structure in the recovery regime is robust to that scatter.

Activation and the reduced-activation intent. The at-or-below-Class-C result with no GTCC waste is the design intent of the RAFM alloy class realised on this machine [28,1]. The reduced-activation substitutions (W, V, Ta for Mo, Nb) are precisely what keeps the long-lived activation products out of the inventory, and the full-chain ALARA calculation confirms the waste-class outcome at the breeder's two-FPY exposure.

Relation to the Kronos series. This qualification sits inside a companion set that shares its frozen anchors. The first-wall and plasma-facing-component lifetime study under 14 MeV loading [33] shares the displacement anchor BR-L1-A13 and treats erosion and bubble swelling for the armour; the component-activation and waste-routing study [34] shares the activation anchor BR-L1-A10 and extends the decommissioning picture; the blanket and divertor thermal-hydraulics study [35] shares the coolant-selection anchor BR-SX-15 and the walk-away case; the first-principles low-activation refractory-alloy screen [36] and the machine-learning-interatomic-potential discovery pipeline [37] extend the composition-screening methodology behind BR-SX-05 to the plasma-facing family. The present paper is the structural-steel node of that network: it takes the same neutron field, the same displacement and helium anchors, and the same first-principles screen, and asks the one question the others do not—does the load-bearing steel clear every gate at once?

§ 8

Limitations

The elastic screen is reduced-order: it establishes Born stability and the Pugh ratio from computed bulk and shear moduli, not from the full anisotropic elastic-constant tensor C_{ij} by finite strain. The complete C_{ij} computation is the one named next step—it was deferred because the density-functional workstation was saturated during the campaign—and, given that the formation energies already reproduce the reference to 0.0 meV/atom, it is expected to confirm rather than overturn the ductility ranking. Separately, the DBTT shift is reported as a model estimate from the published irradiation-temperature dependence, not as a directly computed Kronos anchor; a dedicated hardening-to-embrittlement calculation tied to the machine's own microstructure would replace the estimate with an anchor.

§ 9

Conclusion

A reduced-activation ferritic-martensitic structure qualifies against the coupled load set of the Hyperion compact spherical-tokamak breeder on every gate at once. It holds a peak 516 °C with a 34 °C margin in the self-cooled lithium blanket—a configuration the thermal gate selects over a helium-cooled variant that fails as configured at 712 °C; it stays ductile at Pugh ratios of **1.83–2.22** on formation energies converged to 0.0 meV/atom; it swells only 0.017 as helium accumulates at 226 appm per full-power year, two orders of magnitude below concern and confirmed by two independent methods; it runs at a temperature deep in the DBTT recovery regime, so irradiation embrittlement is not the governing mode; and it decays to Class C or below with no greater-than-Class-C waste—all at a first-wall load of 1.885 MW/m^2 and 18.85 dpa per full-power year. The governing models are written explicitly, the numerics are standard community codes on a reproducible GPU-HPC campaign, and every number is a frozen, auditable anchor. The structural-alloy baseline for the breeder is established on the machine's own numbers.

Acknowledgments tocsectionAcknowledgments Part of the Kronos Fusion Energy 2026 design series. The authors thank the Kronos physics de-risking programme for the frozen result set underlying every quantitative claim.

Reproducibility. The structural-qualification results are frozen anchors in the Kronos Physics De-Risking Register [32] (serials BR-L1-A13, BR-L2-A24, BR-L2-A26, BR-SX-05, BR-SX-15, BR-L1-A9, BR-L1-A10) and are regenerable from the archived input decks with the community codes of table 2; production computation ran on the NVIDIA GPU HPC campaign. This paper is archived at doi:10.5281/zenodo.22645887; official version: https://www.kronosfusionenergy.com/publications/qualifying-reduced-activation-ferritic-martensitic-stee.html and its official version is at https://www.kronosfusionenergy.com/publications/qualifying-reduced-activation-ferritic-martensitic-stee.html; the register is archived at doi:10.5281/zenodo.22133057.

Data availability tocsectionData availability This paper is archived at doi:10.5281/zenodo.22645887. The damage, swelling, elastic-screen, thermal, and activation outputs, and the figure-generation script, are archived with the deposit and reference the Kronos 2026 series and its de-risking register [32] (doi:10.5281/zenodo.22133057). Any economic analysis is reported separately and is not included in the public deposit.

Competing interests tocsectionCompeting interests Provisional patent applications relating to aspects of this work have been filed.

tocsectionReferences

APPARATUS

Portfolio, People & Record

The intellectual-property estate, the people who built it, the limitations that gate it, and the sources it rests on.

1	4	40	27
GRANTED PATENT	2026 PROVISIONALS	TEAM MEMBERS	2022 PROVISIONALS

INTELLECTUAL PROPERTY

The patent portfolio

The estate spans a granted high-field magnet patent, pending utility and 2026 provisional filings that map to the two products, a digital-twin control provisional, a registered trademark application, and the original 2022 provisional family. Every patentable disclosure in the five-paper arXiv drop was protected **before** publication: the breeder and burner provisionals were filed 1–2 August, and a publication-gap omnibus filing the evening before the drop swept up the DEC, plasma-control, and REBCO-winding matter of the three otherwise-unprotected papers. Patent numbers and application serials are matters of public record; claim scope is summarised, not reproduced.

GRANTED & PENDING UTILITY

US 12,009,112	High-field tilted graded-REBCO magnet architecture (KRONO-002A) · *app. 17/878,550*	GRANTED
US 17/878,507	Core device / method (KRONO-001A) · *utility*	PENDING

2026 PROVISIONAL FILINGS — MAPPED TO THE PRODUCTS

64/124,209	Hyperion — spherical-tokamak tritium / helium-3 foundry · *breeder · filed Aug 2026*	FILED
64/124,220	Aegis / MetroVolt — synchrotron-cutoff, fuel-selection & plug-winding · *generator · filed Aug 2026*	FILED
64/115,167	KRONOS-CTRL digital-twin plant control · *provisional · filed Jul 2026*	FILED
64/005,440	Integrated spherical-tokamak fusion architecture · *early integrated-architecture filing · filed Mar 2026*	FILED
64/105,530	Negative-triangularity spherical-tokamak architecture · *foundational ST filing · filed Jul 2026*	FILED
64/128,097	Publication-gap omnibus — quasineutral two-species expander DEC · provenance-gated / latency-split plasma control · as-built high-field winding & conductor architecture · *filed 7 Aug 2026, the evening before the arXiv drop*	FILED

TRADEMARK & ORIGIN

FTK-98801894	Kronos Fusion Energy — trademark application	FILED
KR-2022-*	Original provisional family (KR-2022-00001 … 00027) · *27 filings, 2022*	PRIORITY

The narrow, defensible magnet novelty — the specific conductor and the digital-twin winding optimisation, not high-field REBCO as a category — is the commercial core that can earn ahead of any Q > 1 milestone, with markets in fusion magnet supply, MRI/NMR, accelerators, and proton therapy. The claim is scoped honestly: the high field is a *system field* result, not a stand-alone-coil record; the small-bore plug coil is structurally infeasible as a bare winding but resolved by a stress-managed structural shield (feasible-pending-FEA); and the winding-tape experiment returned a *null result*. The value is the method, not a field record.

THE TEAM

Founding partners, board, advisors & auditors

Kronos is built by a bench of advanced-fuel-fusion, high-field-magnet, direct-conversion, and materials specialists, with a board and operations team drawn from defense, national laboratories, and industry. Dates are shown as ranges; where a tenure has ended or is term-ending, the range says so.

FOUNDING PARTNERS — SCIENCE

Dr. Gerald Kulcinski
Co-Founder · Helium-3 & Advanced-Fuel Fusion
UW–Madison · 2023–Present

Dr. Carl Weggel
Chief Scientist / S.M.A.R.T. Design
MIT Alcator Program · 2022–Present

Dr. Robert J. Weggel
Magnetic Field Design
MIT Magnet Lab · 2022–Present

BOARD

Priyanca Ford
Founder & CEO · Executive Board
2022–Present

Bandel Carano
Finance / Strategy
Oak Investment Partners / Stanford · 2025–2026

Patrick Schweiger
Fusion Device Engineering
Oklo / CFS / TerraPower · 2025–Present

SCIENTIFIC ADVISORS

Dr. Steven O. Dean
Fusion Policy & History
DOE / Fusion Power Associates · 2025–Present

Dr. Patrick H. Diamond
Plasma Turbulence & Transport
UC San Diego · 2025–Present

Dr. Jack J. Dongarra
HPC & Numerical Algorithms
Turing Award · 2025–Present

Dr. Nasr M. Ghoniem
Chief Material Scientist
UCLA · 2025–Present

Dr. Siegfried Glenzer
Plasma Physics & Laser Fusion
Stanford / SLAC · 2022–Present

Dr. David A. Hammer
Pulsed-Power Fusion
Cornell · 2025–Present

Dr. Donald A. Spong
Plasma Theory & Confinement
ORNL · 2025–Present

Dr. Curtis Smith
Risk Assessment & Nuclear PRA
MIT / Idaho National Lab · 2025–Present

RADM (Ret.) David Goggins
Naval Engineering & Power-Plant Design
U.S. Navy · 2023–2026

Dr. Konstantin Batygin
Mathematician
Caltech · 2022–2025

Dr. Ruben Fair
Magnet Design / ITER Liaison
PPPL / Jefferson Lab · 2022–2025

Dr. Paul S. Weiss
Materials & Nanotechnology
UCLA · 2022–2025

SCIENTIFIC AUDITORS

Dr. Wilfred A. Cooper
Plasma Equilibrium Theory
EPFL / Swiss Plasma Center · 2025–Present

Dr. Ahmed Hassanein
Plasma–Material Interactions
Purdue / Argonne · 2025–Present

Dr. Patrick E. Hopkins
Extreme Thermal Materials
U. of Virginia · 2025–Present

Dr. Peter Hosemann
Materials Joining & Structural Integrity
UC Berkeley · 2025–Present

Dr. Travis W. Knight
Advanced Nuclear Fuels & Systems
U. of South Carolina · 2025–Present

Dr. Philippe Lebrun
Cryogenics & Magnet Cooling
CERN · 2025–Present

Dr. Nitendra Singh
Nuclear Safety & Fuel Cycle
ITER · 2025–Present

Dr. Guido Van Oost
Magnetic Confinement & Fusion Systems
Ghent University · 2025–Present

Dr. Gary S. Was
Radiation Materials & Structural Integrity
U. of Michigan · 2025–Present

Dr. Ray Sedwick
Direct Energy Conversion
U. of Maryland · 2025

OPERATIONS

Michael Laughlin
Chief Operating Officer
2022–Present

Martin Owens
Chief Strategy Officer
LANL / GE Hitachi · 2022–Present

MG (Ret.) Paul Pardew
Chief Contracting Officer
Army Contracting Command · 2022–Present

David Beck
Fusion Commercialization
U.S. Space Force · 2024–Present

Sushma Bhatia
Environmental & Legislative
Google · 2022–Present

Michael De Frenza
Technology Licensing
2023–Present

MG (Ret.) Robin L. Fontes
Cybersecurity & Defense
Army Cyber Command · 2022–Present

Vijay Gehani
Supply Chain & Components
INOX India · 2024–Present

Jon Michel Greenwood
IT & AI Infrastructure
Live Nation · 2023–Present

Brian C. O'Neill
National Security
CIA / ODNI · 2022–Present

Gen. (Ret.) Gustave F. Perna
DoD Liaison
Operation Warp Speed · 2022–2023

Andrea Romero
Marketing Lead
2022–Present

Legal counsel is retained; those roles are held on the internal roster and are not listed here.

SOURCES

References

1 S J Zinkle and G S Was, Materials challenges in nuclear energy, *Acta Mater.* **61** 735 (2013). doi:10.1016/j.actamat.2012.11.004

2 E E Bloom, The challenge of developing structural materials for fusion power systems, *J. Nucl. Mater.* **258–263** 7 (1998).

3 N Baluc *et al*, Status of R&D activities on materials for fusion power reactors, *Nucl. Fusion* **47** S696 (2007).

4 R L Klueh and A T Nelson, Ferritic/martensitic steels for next-generation reactors, *J. Nucl. Mater.* **371** 37 (2007).

5 R Lindau *et al*, Present development status of EUROFER and ODS-EUROFER for application in blanket concepts, *Fusion Eng. Des.* **75–79** 989 (2005).

6 H Tanigawa *et al*, Development of benchmark reduced activation ferritic/martensitic steels for fusion energy applications, *Nucl. Fusion* **57** 092004 (2017).

7 D Stork *et al*, Materials R&D for a timely DEMO: key findings and recommendations of the EU Roadmap Materials Assessment Group, *Fusion Eng. Des.* **89** 1586 (2014).

8 G R Odette, M J Alinger and B D Wirth, Recent developments in irradiation-resistant steels, *Annu. Rev. Mater. Res.* **38** 471 (2008).

9 P Yvon and F Carr\'e, Structural materials challenges for advanced reactor systems, *J. Nucl. Mater.* **385** 217 (2009).

10 J E Menard *et al*, Fusion nuclear science facilities and pilot plants based on the spherical tokamak, *Nucl. Fusion* **56** 106023 (2016). doi:10.1088/0029-5515/56/10/106023

11 B N Sorbom *et al*, ARC: a compact, high-field, fusion nuclear science facility and demonstration power plant with demountable magnets, *Fusion Eng. Des.* **100** 378 (2015). doi:10.1016/j.fusengdes.2015.07.008

12 M J Norgett, M T Robinson and I M Torrens, A proposed method of calculating displacement dose rates, *Nucl. Eng. Des.* **33** 50 (1975).

13 K Nordlund *et al*, Improving atomic displacement and replacement calculations with physically realistic damage models, *Nat. Commun.* **9** 1084 (2018).

14 M R Gilbert *et al*, Neutron-induced dpa, transmutations, gas production, and helium embrittlement of fusion materials, *J. Nucl. Mater.* **442** S755 (2013).

15 H Trinkaus and B N Singh, Helium accumulation in metals during irradiation—where do we stand?, *J. Nucl. Mater.* **323** 229 (2003).

16 H Ullmaier, The influence of helium on the bulk properties of fusion reactor structural materials, *Nucl. Fusion* **24** 1039 (1984).

17 G S Was, *Fundamentals of Radiation Materials Science: Metals and Alloys*, 2nd ed. (Springer, New York, 2017).

18 S F Pugh, Relations between the elastic moduli and the plastic properties of polycrystalline pure metals, *Philos. Mag.* **45** 823 (1954).

19 F Mouhat and F-X Coudert, Necessary and sufficient elastic stability conditions in various crystal systems, *Phys. Rev. B* **90** 224104 (2014).

20 M Born, On the stability of crystal lattices. I, *Math. Proc. Cambridge Philos. Soc.* **36** 160 (1940).

21 P K Romano, N E Horelik, B R Herman, A G Nelson, B Forget and K Smith, OpenMC: a state-of-the-art Monte Carlo code for research and development, *Ann. Nucl. Energy* **82** 90 (2015). doi:10.1016/j.anucene.2014.07.048

22 A P Thompson *et al*, LAMMPS—a flexible simulation tool for particle-based materials modeling at the atomic, meso, and continuum scales, *Comput. Phys. Commun.* **271** 108171 (2022).

23 S Plimpton, Fast parallel algorithms for short-range molecular dynamics, *J. Comput. Phys.* **117** 1 (1995).

24 R E MacFarlane, D W Muir, R M Boicourt, A C Kahler and J L Conlin, *The NJOY Nuclear Data Processing System, Version 2016*, Los Alamos National Laboratory report LA-UR-17-20093 (2017).

25 J-Ch Sublet, J W Eastwood, J G Morgan, M R Gilbert, M Fleming and W Arter, FISPACT-II: an advanced simulation system for activation, transmutation and material modelling, *Nucl. Data Sheets* **139** 77 (2017).

26 P Giannozzi *et al*, QUANTUM ESPRESSO: a modular and open-source software project for quantum simulations of materials, *J. Phys.: Condens. Matter* **21** 395502 (2009).

27 J P Perdew, K Burke and M Ernzerhof, Generalized gradient approximation made simple, *Phys. Rev. Lett.* **77** 3865 (1996).

28 S Fetter, E T Cheng and F M Mann, Long-term radioactivity in fusion reactors, *Fusion Eng. Des.* **6** 123 (1988).

29 M Abdou *et al*, Blanket/first wall challenges and required R&D on the pathway to DEMO, *Fusion Eng. Des.* **100** 2 (2015).

30 G Federici *et al*, Overview of the design approach and prioritization of R&D activities towards an EU DEMO, *Fusion Eng. Des.* **109–111** 1464 (2016).

31 J Marian *et al*, Recent advances in modeling and simulation of the exposure and response of tungsten to fusion energy conditions, *Nucl. Fusion* **57** 092008 (2017).

32 P I Ford, *Kronos Physics De-Risking Register*, Kronos Fusion Energy 2026 series. doi:10.5281/zenodo.22133057

33 P I Ford, First-wall and plasma-facing-component lifetime under 14 MeV loading: displacement damage, bubble swelling and erosion in a compact spherical-tokamak breeder, Kronos Fusion Energy 2026 series. doi:10.5281/zenodo.22645774. https://www.kronosfusionenergy.com/publications/first-wall-neutron-damage-lifetime.html

34 P I Ford, Component activation, waste-class routing, and decommissioning of a low-activation compact spherical-tokamak breeder, Kronos Fusion Energy 2026 series. doi:10.5281/zenodo.22645846. https://www.kronosfusionenergy.com/publications/component-activation-waste-class-routing-and-decommissi.html

35 P I Ford and G L Kulcinski, Blanket and divertor thermal-hydraulics for a compact spherical-tokamak breeder: coolant heat removal, peak-temperature margins, and the walk-away safety case, Kronos Fusion Energy 2026 series. doi:10.5281/zenodo.22645836. https://www.kronosfusionenergy.com/publications/blanket-and-divertor-thermal-hydraulics-for-a-compact-s.html

36 P I Ford and G L Kulcinski, First-principles near-neutral low-activation refractory alloys for fusion plasma-facing components, Kronos Fusion Energy 2026 series. doi:10.5281/zenodo.22645744. https://www.kronosfusionenergy.com/publications/low-activation-alloys.html

37 P I Ford, A machine-learning interatomic-potential to activation-transport pipeline for low-activation fusion alloy discovery, Kronos Fusion Energy 2026 series. doi:10.5281/zenodo.22645797. https://www.kronosfusionenergy.com/publications/ml-potential-materials-discovery-pipeline.html

COLOPHON

How this document was made

The Kronos Fleet — Combined Editorial, 2026 is set in **Fraunces** (display), **Gelasio** (text), and **IBM Plex Mono** (data & equations), carried forward from the Kronos editorial design system.

The figures are rendered at 300 dpi from the deposited generator scripts; the document is composed as a single self-contained file with embedded fonts and imagery, paginated to US Letter, and rendered to PDF through a headless Chromium engine in matched light and dark editions.

Every headline quantity carries an evidence class; withdrawn and restated values are marked as such. Nothing herein is frozen beyond the founder-approved Tier-A set.

Explore it live — turn the interactive 3-D model, run the deposited solvers in the physics validator, and watch the companion film series.

LEGAL NOTICE

Notice, status, and distribution

Conceptual design & simulation study. This document reports a conceptual design and simulation study. It is not a construction commitment, a safety-analysis report, a regulatory filing, or an offer of securities. Forward-looking statements — schedules, costs, market sizes, and performance — are estimates subject to the limitations set out in the Simulations part and may change.

Numbers and their classes. Quantities are reported with evidence classes and case labels; modelled, assumed, and requirement-class values are identified as such and are not to be quoted without their labels.

Public edition. This edition carries the physics and design only; all financial, funding, and defense-commercial content has been removed for public distribution. The scientific text corresponds to the arXiv and journal submissions.

THE 2026 KRONOS SERIES

One programme, many papers

This editorial is one paper in the Kronos 2026 series — a real fusion company's complete, reproducible physics record for a spherical-tokamak breeder and its low-neutron D–^{3}He tandem-mirror burners. Every headline number is a frozen anchor in the Physics De-Risking Register.

Explore the whole programme: the De-Risking Register, the interactive 3-D model, and the physics validator.

KRONOS FUSION ENERGY

Qualifying Reduced-Activation Ferritic-Martensitic Steel for a Compact Spherical-Tokamak Breeder: Strength, DBTT Shift and Swelling under 14 MeV Neutron Loading

A real fusion company building real machines. Explore the science, live.

Zenodo · doi:10.5281/zenodo.22645887

Read on kronosfusionenergy.com

The Physics De-Risking Register